UC Irvine
UC Irvine Previously Published Works

Title
CHARACTERIZATION AND CLASSIFICATION OF SEA ICE IN POLARIMETRIC SAR DATA

Permalink
https://escholarship.org/uc/item/8g73137f

Authors
KWOK, R
DRINKWATER, M
PANG, A
et al.

Publication Date
1991

Copyright Information

Peer reviewed

CHARACTERIZATION AND CLASSIFICATION OF SEA ICE IN POLARIMETRIC SAR DATA

R. Kwok, M. Drinkwater, A. Pang and E. Rignot

Jet Propulsion Laboratory
California Institute of Technology
Pasadena, CA 91109
Telex 675-429
FAX (818) 393-6943
Ph (818) 354-5614

Abstract

Some of the first examples of multi-frequency, polarimetric SAR signatures of sea ice were presented in Kwok [1] and Drinkwater et al. [2, 3]. These signatures were derived from data acquired in the Beaufort, Bering and Chukchi Seas in March 1988 during a campaign for validation of the DMSP SSM/I radiometer ice products. These preliminary observations suggested potential enhancement of our capability to discrimate sea ice types in SAR data. The focus of this work is to provide a more detailed characterization of the signatures of apparent thin ice types observed in these data and the utility of these signatures for ice type classification purposes. The statistical characteristics of these signatures and the dependence of them on system calibration are summarized. Implications of these observations for sea ice scattering models are briefly discussed.

Keywords: *Sea-Ice Polarimetry, Ice Signatures*

1. Introduction

Turbulent heat flux from the ocean to the atmospheric boundary layer is a function of sea ice thickness with an especially strong dependence on sea ice with thicknesses in the 0-100cm range [4]. Within this range, the flux can increase by at least an order of magnitude as the thickness approaches zero. It is quite difficult to discriminate the different types of thin ice based entirely on backscatter in single frequency and polarization SAR. Potential enhancement of our ability to discriminate different ice types in multi-frequency, multi-polarization has been pointed out in [1, 2, 3]. Some examples of the polarization signatures of sea ice were provided in [2, 3]. The focus of this work is to provide a more detailed characterization of the apparent thin ice types in the multi-frequency, multi-polarization SAR dataset acquired during the DMSP SSM/I validation campaign. Some of the effects of the statistics of polarimetric parameters and system calibration on ice signature estimation are discussed. These effects are especially significant for targets with microwave responses close to the noise level of the radar. Young and smooth ice types fall into this category due to their smooth upper surface and high reflectivity.

Section 2 gives a brief description of the dataset and the regions of open water/thin-ice which have been selected for analysis. The calibration of these data is also described. Polarimetric parameters which are used for characterizing these ice types are provided in Section 3. and the statistical properties of these parameters and their dependence on system noise performance are discussed. Signatures of the open water/thin ice types are described in Section 4 and a summary is provided in Section 5.

2. Data Description

During March 1988, multi-frequency polarimetric SAR data were acquired over the Beaufort, Chukchi and Bering seas using the NASA DC-8 airborne laboratory. The radar operates in the C-, L- and P- bands (5.31, 1.26, 0.45 GHz respectively). Each frequency channel has the capability of simultaneously collecting linear like-polarized (HH and VV) and cross-polarized (HV and VH) backscatter data. The complete polarization signature of every resolution element in an image is recorded. Additionally, the radiometric and polarimetric data samples are processed such that they are spatially registered. The spatial resolution of the SAR data is approximately 6.6m in range and 11m in the azimuth direction. The range of look angles of the radar is between 0 and 70°.

Sea Ice Dataset/Regions of Interest
Two L-band total power images were selected for examination of open water/thin ice signatures, these are shown in Figures 1 (ID = CM1372) and 2 (ID = CM0291). Both datasets were acquired during flights over the Beaufort Sea on March 11, 1988. A mixture of first-year (FY) and multi-year (MY) ice of various ages can be observed in both images. On the left hand side of the image in Fig. 1, there are several openings with relatively low backscatter which is indicative of open water or relatively new or thin young ice. The signature of the open water/thin ice in the leads is discussed further in the next section. The image in Fig. 2 was acquired several hours after the first and is further north into the Beaufort Sea. Again the distinctive signatures of MY and FY under Arctic winter conditions can be easily recognized 1, 2, 3. The thin ice region of interest possesses radiometric signatures relatively similar to that of thick FY-ice in L-band but has multi-frequency and polarimetric signatures quite distinctive from apparently thicker
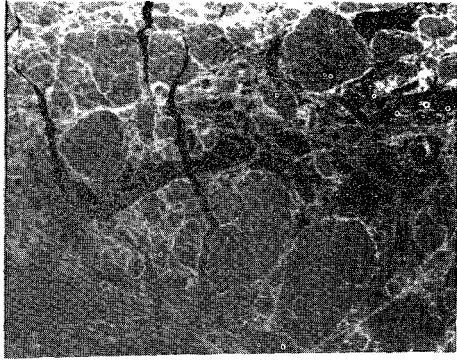
81

Fig. 1. L-band total power image of CM1372.

Fig. 2. L-band total power image of CM0291.

FY ice. The relatively high backscatter of this area in C-band compared to L-band can be easily constrasted to the behavior of thick FY ice in the total power images from the same area (Figure 3a and 3b). Again, the signature of this region is discussed further in the next section.

Data Calibration
The polarimetric characteristics for the radar flown during the 1988 Alaska campaign were quite stable at L-band, although less so at C-band and P-band. The polarimetric calibration of the radar was assessed during an over-flight of trihedral corner reflectors deployed at the Fairbanks airport during one day of the campaign (March 13) [5]. From the trihedral measurements, the gain imbalance (VV/HH) between the two co-polarized channels, were -1.8dB, -0.6dB for C- and L-bands. respectively and the cross-channel isolation of C- and L-bands were -27dB and -17dB, respectively Cross channel isolation affects the sensitivity of the radar to the cross-pol (hv) returns from the sea-ice.

The datasets used in this work were phase-calibrated to remove the instrument-induced errors in the phase relationship between the radar channels. Calibration is accomplished by selecting an in-scene target where the scattering phase difference between $hh - vv$ is known and using this knowledge to remove the phase offset between the channels. Sample windows within a multi-year floe in each image were selected as polarimetric phase references with $\phi_{vvhh} = 0$. Examination of this polarimetric phase in MY and FY ice indicate that they are approximately the same i.e. ~ 0 and that one could have selected FY as well MY ice as phase calibration targets.

3. Data Analysis

The multi-frequency polarimetric data distributed by JPL is stored in a compressed Stokes matrix format. The reconstructed Stokes matrix at each spatial sample is a 4x4 symmetric real matrix representing the polarimetric backscatter properties for an area of the surface at that incidence angle. Two polarimetric quantities (derived from these Stokes matrices) other than the co-pol and cross-pol backscatter cross-sections ($\sigma_{hh}, \sigma_{vv}, \sigma_{hv}$), which are used here to characterize the specific ice types, are the polarization ratio, γ and the polarization correlation coefficient, ρ, where:

$$\gamma = \frac{< |VV|^2 >}{< |HH|^2 >},$$
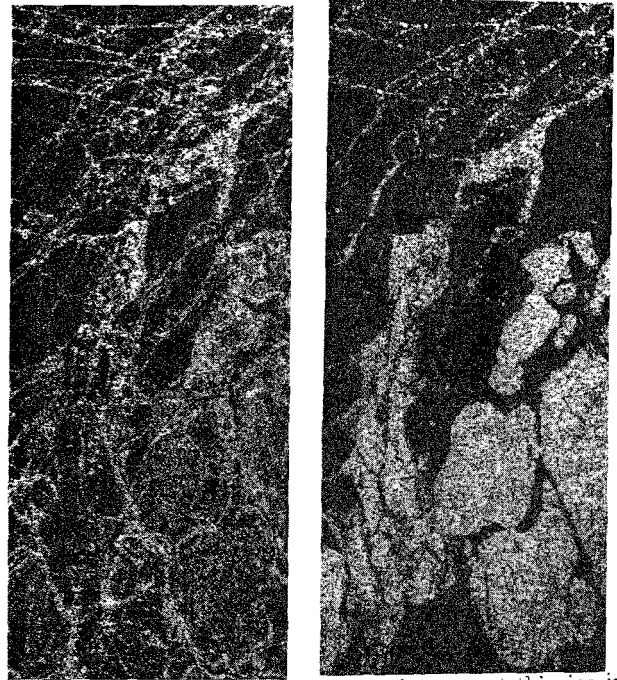

Fig. 3. Multi-frequency signature of apparent thin ice in CM0291. (a) L-band total power image. (b) C-band total power image.

$$\rho = < HH\ VV^* > .$$

$|\rho|$ is the correlation between the VV and HH returns and $\angle\rho$ is the phase difference between VV and HH returns.

Statistical Characteristics of $\frac{|VV|^2}{|HH|^2}$
The probability density function of the ratio of the magnitudes ($\frac{|VV|}{|HH|}$) is described in Kong [6]. Based on this density function. the corresponding density function of the polarization ratio, ($y = \frac{|VV|^2}{|HH|^2}$) can be obtained using a straightforward transformation of $y = r^2$ resulting in,

$$PDF(y) = \frac{\gamma(1 - \rho^2)(\gamma - y)}{((\gamma + y)^2 - 4\gamma y \rho^2)^{3/2})}$$

which is dependent on the polarization ratio, γ and the correlation, $|\rho|$, between HH and VV returns from the target. Figure 4 shows the density function of the power ratio y for $\gamma = 1.5$ and 3.0 with $|\rho| = 0.7$. It can be seen that the width of the density function (or variance) is proportional to γ of the target giving the density function a rather long tail for large values of γ. Effectively, a larger sample population is required to provide equivalently good estimates of the mean γ of a target with a large expected γ.
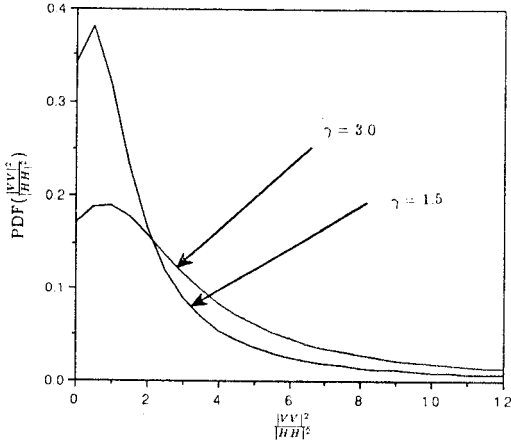
Fig. 4. Density function of the $y = \frac{|VV|^2}{|HH|^2}$.

Fig. 5. Dependence of $|\rho|$ on signal-to-noise ratio and polarization ratio.

Sensitivity of γ to System Noise

Since the thin ice/open water backscatter signatures are fairly low (less than 5dB) compared to the system noise level, the effect of the system noise level on the estimates of γ is discussed here. System noise contribution to the expected target backscatter cross-sections tend to cause an underestimation of γ, viz.

$$\frac{< |VV + n|^2 >}{< |HH + n|^2 >} \leq \frac{< |VV|^2 >}{< |HH|^2 >}$$

Therefore, the removal of the system noise contribution is required for accurate estimation of γ. L-band data acquired by the NASA/JPL SAR has a noise floor at approximately -40dB, which remains constant across the range swath and the C-band data has a noise floor which is range dependent and is approximately -35dB at boresight [7].

Sensitivity of ρ to System Noise

System noise contribution tend to decorrelate the HH and VV responses, again causing an underestimation of the correlation coefficient, $|\rho|$, if this noise level is not accounted for. The dependence of the correlation coefficient, ρ, on the signal-to-noise performance of the radar. assuming $< n_h n_v > = 0$, can be written as,

$$\rho_{actual} = \rho_{measured} \frac{(SNR_{HH} + 1)(\gamma SNR_{HH} + 1)^{1/2}}{\gamma^{1/2} SNR_{HH}}$$

$$= f(SNR_{HH}, \gamma)$$

where SNR_{HH} is the signal-to-noise ratio of the HH channel. Figure 5 is a plot $f(SNR_{HH}, \gamma)$ which shows the dependence of the scale factor f on SNR_{HH} for different realization of target γ. As expected this factor approaches one with increasing SNRs.

4. Ice Signatures

Open Water/Thin Ice in CM1372

Winebrenner [8] suggested using the polarization ratio behavior (at L-band) to discriminate between thin ice and open water. This was accomplished by comparing the polarization ratio generated using a first-order Bragg rough surface scattering model for seawater and thin ice with the radar observations. Following this procedure, a plot of the γ vs incidence angle behavior of the data samples in the leads is shown in Fig. 6. Each γ is estimated from a
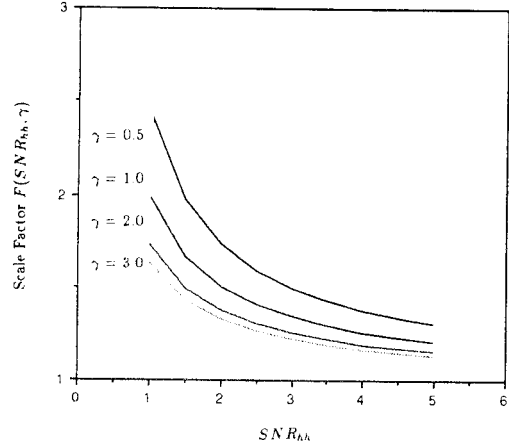
window of approximately 20x20 samples. The model behavior for the seawater ($\epsilon = 76.3 + i55.97$) and thin ice ($\epsilon = 3.95 + i0.5$) responses at L-band are overlayed on the same plot. The data showed fairly good correspondence with the model predictions in the near range, however, a slight divergence (decrease in the observed slope) can be observed which could be an effect caused by system noise. Figure 7 shows the same plot after the system noise contribution has been removed. It showed that slope in the far range has increased somewhat and that the data are closer to the theoretical behavior for seawater rather that thin ice. Evidence of open water/thin ice can be observed in the K_a-band scanning radiometer (KRMS) image data of the same ice (not shown here) which were acquired roughly 10 minutes before of the DC-8 SAR. The brightness temperature of the apparent ice/water in the leads is approximately $150°K$ compared to the MY brightness temperature of $170°K$ and is indicative of open water or new ice [9].

Thin ice in CM0291

The apparent thin ice type shown in Figure 3 has been observed in several images acquired during the Alaska campaign. This ice type has a very characteristic high backscatter (approaching that of MY ice) at C-band and relatively low backscatter at L-band. Polarimetrically, this ice type causes a fairly significant phase shift ($\phi_{VV-HH} = -15°$ to $-20°$) between the VV and HH returns at L-band with insignificant phase shifts at C-band. Figure 8 shows the polarization phase shift vs incidence angle plot of this ice type at L-band and C-band. The correlation coefficient $|\rho|$ of 0.6-0.7 is lower that that observed for FY and MY ice at L-band and is comparable to FY and MY ice at C-band. The multi-frequency polarization signatures suggest that this ice type appears as a fairly lossy dielectric with a rough surface at C-band. At L-band, the relatively higher cross-pol return suggests volume scattering contribution from the medium with the phase shift being caused by boundaries of the thin ice layer. Currently, the observed phase shift cannot be explained by an infinitely thick ice layer. It is speculated that these surfaces are roughened at their upper surface by frost flowers which have significant salt content, thus explaining the wavelength dependency in the rough surface scattering which is observed.
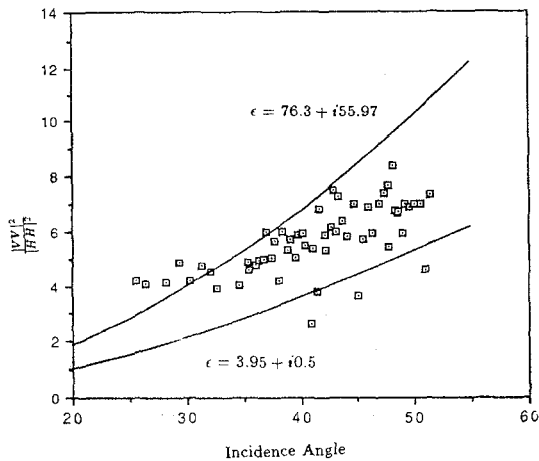
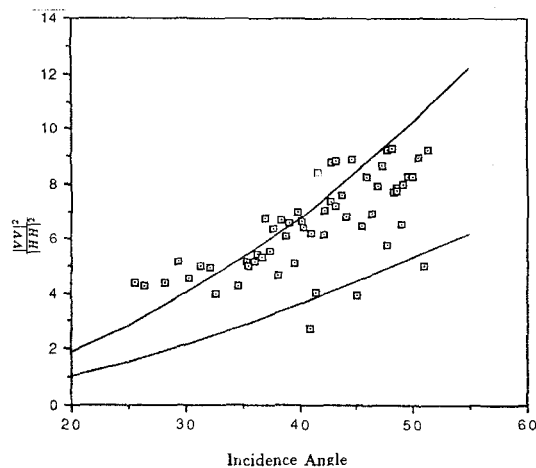Fig. 6. Polarization ratio (dB) vs incidence angle (deg) behavior of ice in leads.

Fig. 7. Corrected polarization ratio (dB) vs incidence angle (deg) behavior of ice in leads.

5. Summary

Multi-frequency polarimetric signatures of some thin ice types are presented. The effect of the statistical characteristics and system noise performance on the estimation of these polarization signatures are treated. Corrections are suggested on the basis of noise estimates, which improves the results. Observations from remotely-sensed polarimetric data (without the benefit of direct field measurements) are important not only for characterizing the sea ice discrimination capability with polarimetric data but also for determining the focus for field experiments and model efforts for studying these observed signatures.
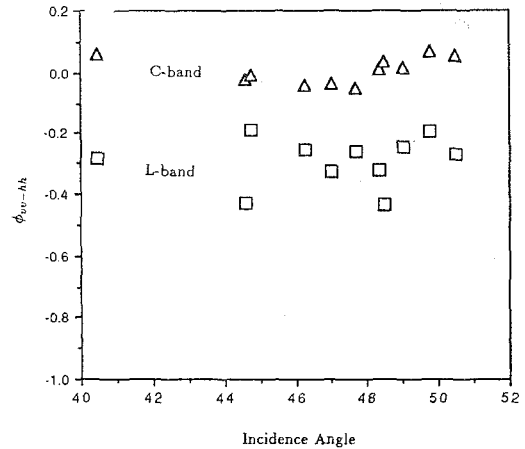
Acknowledgments

Fig. 8. Dependence of phase shift ϕ_{vv-hh} (deg) on incidence angle.

References

1. Kwok, R. and M. Drinkwater. Multi-frequency Polarimetric Observations of Sea Ice. Presented at *URSI - Signature Problems in Microwave Remote Sensing of the Surface of the Earth*, Hyannis, MA, 1990.

2. Drinkwater, M., R. Kwok, D. Winebrenner and E. Rignot. Multi-frequency Polarimetric SAR Observations of Sea Ice, 1990. Submitted to JGR.

3. Drinkwater, M., R. Kwok and E. Rignot. Synthetic Aperture Radar Polarimetry of Sea Ice. *Proceedings of IGARSS'90*, College Park, MD.

4. Maykut, G. A. The Surface Heat and Mass Balance. In *The Geophysics of Sea Ice*. Ed. N. Untersteiner. Plenum Press.

5. Freeman, A., A Calibration and Image Quality Assessment of the NASA/JPL Aircraft during Spring 1988 using Trihedral Corner Reflectors. Submitted to *IEEE Trans. Geosci. Rem. Sens.*

6. Kong, J., A. A. Swartz, H. A. Yueh, L. M. Novak and R. T. Shin. Identification of Terrain Cover Using Optimum Polarimetric Classifier. *J. of Electrom. Waves and Applic.*, Vol. 2., No. 2, pp. 171-194, 1988.

7. Freeman, A. Personal Communication, 1991.

8. Winebrenner, D. P., Accuracy of Thin Ice/Open Water Classification using Multi-polarization SAR. *Proceedings of IGARSS'89*, Vancouver, B.C.

9. Eppler, D., L. D. Farmer, A. W. Lohanick and M. Hoover. Digital Processing of Passive K_a-band microwave images for Sea Ice Classification. NORDA, Stennis Space Center, Mississippi, NORDA Report 51.